RESEARCH ARTICLE

Key Points:
- Meridional distributions of protons and pressure-driven currents in the nightside inner magnetosphere are first obtained by Arase
- Plasma pressure, plasma beta, and pressure-driven currents significantly decrease with increasing magnetic latitude
- The latitudinal dependence should be taken into account in interpretations of plasma parameters in successive orbits during magnetic storms

Correspondence to:
S. Imajo,
imajos@isee.nagoya-u.ac.jp

Meridional Distribution of Middle-Energy Protons and Pressure-Driven Currents in the Nightside Inner Magnetosphere: Arase Observations

S. Imajo[1] [ID]**, M. Nosé[1]** [ID]**, S. Kasahara[2]** [ID]**, S. Yokota[3]** [ID]**, A. Matsuoka[4]** [ID]**, K. Keika[2]** [ID]**, T. Hori[1]** [ID]**, M. Teramoto[1]** [ID]**, K. Yamamoto[5]** [ID]**, S. Oimatsu[5]** [ID]**, R. Nomura[6]** [ID]**, A. Fujimoto[7]** [ID]**, I. Shinohara[4]** [ID]**, and Y. Miyoshi[1]** [ID]

[1]Institute for Space-Earth Environmental Research, Nagoya University, Nagoya, Japan, [2]Graduate School of Science, University of Tokyo, Tokyo, Japan, [3]Graduate School of Science, Osaka University, Toyonaka, Japan, [4]Institute of Space and Astronautical Science, Japan Aerospace Exploration Agency, Sagamihara, Japan, [5]Graduate School of Science, Kyoto University, Kyoto, Japan, [6]National Astronomical Observatory of Japan, Mitaka, Japan, [7]Faculty of Computer Science and Systems Engineering, Kyushu Institute of Technology, Iizuka, Japan

Abstract We examined the average meridional distribution of middle-energy protons (10–180 keV) and pressure-driven currents in the nightside (20–04 hr magnetic local time) ring current region during moderately disturbed times using the Arase satellite's data. Because the Arase satellite has a large inclination orbit of 31°, it covers the magnetic latitude (MLAT) in the range of −40° to 40° and a radial distance of $< 6R_E$. We found that the plasma pressure decreased significantly with increasing MLAT. The plasma pressure on the same L^* shell at 30° < MLAT < 40° was ~10–60% of that at 0° < 4 MLAT < 10°, and the rate of decrease was larger on lower L^* shells. The pressure anisotropy, derived as the perpendicular pressure divided by the parallel pressure minus 1, decreased with radial distance and showed a weak dependence on MLAT. The magnitude of the plasma beta at 30°< MLAT < 40° was 1 or 2 orders smaller than that at 0°< MLAT < 10°. The plasma pressure normalized by the value at 0°< MLAT < 10° estimated from the magnetic strength and anisotropy was roughly consistent with the observed plasma pressure for $L^* = 3.5$–5.5. The azimuthal pressure-gradient current derived from the plasma pressure was distributed over MLAT ~ 0–20° , while the curvature current was limited within MLAT ~ 0–10° . We suggest that the latitudinal dependence should be taken into account in interpretations of plasma parameters in successive orbits during magnetic storms.

1. Introduction

The inner magnetosphere is the region where the plasma thermal pressure is highest in the near-Earth space during magnetic storms. The plasma pressure is mainly contributed by protons in an energy range of 10 to 300 keV (e.g., Daglis et al., 1993; Jordanova & Miyoshi, 2005; Williams, 1981; Zhao et al., 2015). Peak plasma pressure is usually located at ~3–4 R_E, depending on the energy range of the instruments used and geomagnetic activities (e.g., De Michelis et al., 1999; Lui et al., 1987). Plasma pressure drives large-scale azimuthal currents both inside and outside of the peak, the so-called ring current. Enhancement of the ring current is a typical feature of magnetic storms which is characterized by the large depression of ground magnetic fields. The ring current also distorts the background magnetic field in the magnetosphere, resulting in the modification of plasma parameters, such as plasma pressure, plasma anisotropy, and plasma beta. Changes in the magnetic field and plasma parameters modify not only the ring current itself but also the characteristics of plasma instabilities and waves. For example, the plasma beta is an important factor for the growth rate of the mirror instability (e.g., Chandrasekhar et al., 1958), and plasma anisotropy determines the occurrence of electromagnetic ion cyclotron waves (e.g., Cornwall et al., 1970). Therefore, the distribution of background magnetic fields, currents, and plasma have an impact on studies of various phenomena in the inner magnetosphere.

The L value (or radial distance) dependence of the plasma pressure (or energy density) has been examined by numerous studies since early in situ observations (see review by Williams, 1981). The average distributions of plasma parameters in the L-MLT (L-magnetic local time) plane near the magnetic equator have been

investigated by using data from the Active Magnetospheric Particle Tracer Explorer/Charge Composition Explorer satellite. De Michelis et al. (1999) investigated average L-MLT distributions of proton plasma pressure and anisotropy in the energy range of 1–300 keV obtained by the Charge-Energy-Mass spectrometer. Lui (2003) combined the particle measurements from two instruments, the Charge-Energy-Mass spectrometer and Medium Energy Particle Analyzer, with an energy range of 1 keV to 4 MeV, and presented the average L-MLT distributions of proton and oxygen plasma pressures. Ebihara et al. (2002) examined L-MLT distributions near the equatorial plane of proton energy density in the energy range of 1–200 keV for storm stages, using data from the Polar satellite; they found a strong day-night asymmetry in energy density during the main phase. Energetic neutral atom imaging on board the Imager for Magnetopause-to-Aurora Global Exploration satellite captured the global plasma pressure distribution at a specific time, although the energy range (10–120 keV) and spatial resolution were limited (C:son Brandt et al., 2004; Roelof, 1989; Roelof et al., 2004). Recently, Yue et al. (2018) conducted a comprehensive study of the L-MLT distribution of plasma pressures for each species, energy range, and AE index level using data from the Van Allen Probes. The satellites used in these previous studies had low-inclination orbits ($< 10°$), and their magnetic latitudes (MLATs) were within $\pm 20°$ except for the Polar satellite. There is little information available on plasma parameters in the inner magnetosphere at |MLAT| higher than 20°.

Although the L-MLT distributions of plasma parameters have been well studied, little attention has been paid to their meridional or latitudinal distributions. When particle pitch angle (α) distributions have a peak at 90° at the magnetic equator, the so-called pancake distribution, such anisotropy is typical in the inner magnetosphere (Garcia & Spjeldvik, 1985; Shi et al., 2016; Sibeck et al., 1987); some of these particles cannot reach satellites located in the off-equatorial plane. This means that the measured particle flux and pressure becomes smaller as the MLAT of a satellite increases. The pancake distribution is often modeled by the function $\sin^{\gamma}\alpha$ (e.g., Shi et al., 2016; Summers & Shi, 2015), where γ is a power index to show the plasma anisotropy. According to the theory of field-aligned particle distribution in static equilibrium (Parker, 1957), when the pitch angle distribution can be expressed by $\sin^{\gamma}\alpha$, the particle flux decreases with $[B/B_{eq}]^{-\frac{\gamma-1}{2}}$ along the field line, where B/B_{eq} is the magnetic strength normalized by its value at the magnetic equator. This can affect the distribution of plasma parameters as a function of L value if they vary significantly with MLAT. Because the angle between the Earth's rotational axis and the magnetic dipole axis is $\sim 10°$, the MLAT of medium Earth orbit satellites can vary by $\sim 20°$ at most from orbit to orbit. To examine the temporal evolution of ring current particles during magnetic storms, many previous studies have examined the time sequence of L value distributions in successive orbits. Therefore, how the MLAT of a satellite affects the measured plasma parameters is an important issue for the study of magnetic storms.

The meridional distribution of currents in the inner magnetosphere has been examined using the curl of the average distribution of the measured magnetic field (Jorgensen et al., 2004; Le et al., 2004). These studies showed that the ring current extends to the off-equatorial regions. The L-MLT distribution of the ring current has also been derived from the plasma pressure distribution (De Michelis et al., 1997, 1999; Imajo et al., 2018; Lui et al., 1987; Lui & Hamilton, 1992; McEntire et al., 1985); however, its meridional distribution has not been obtained from the plasma pressure since the meridional distribution of plasma pressure has not yet been investigated. An advantage of using plasma pressure is that we can separately evaluate the contribution of the pressure-gradient and curvature currents (will be described in the next section). Previous studies have shown that near the magnetic equator, the curvature current flows eastward around the pressure peak region, and its magnitude is smaller than that of the pressure-gradient current (e.g., Lui et al., 1987). However, differences among the meridional distributions of these current components have not been addressed.

In this study, we investigated the average meridional distributions of proton plasma parameters in the nightside inner magnetosphere using particle and magnetic field measurements from the Exploration of Energization and Radiation in Geospace satellite, now known as the Arase satellite. Because the Arase satellite has a large inclination of 31°, it covers an MLAT range of −40° to 40° and a radial distance of up to 6 R_E. We calculated the meridional distributions of the pressure-gradient and curvature currents from the observed plasma pressure and magnetic field distributions. In section 4, we compare latitudinal variations in the plasma pressure using particle measurements with those estimated from the theory of field-aligned

particle distribution. Based on the observational results, we demonstrate that the MLAT dependence is significant in spatial distribution of plasma parameters and currents.

2. Analysis

2.1. Data Descriptions

The Arase satellite, launched in December 2016, has an elliptical orbit with a perigee of 400 km, an apogee of 32,000-km altitude, and an inclination of 31° (Miyoshi et al., 2018). The spin period is ∼8 s, and the orbital period is ∼9.5 hr. We used data from when Arase was located on the nightside of 20–4 hr MLT during the period from 16 May 2017 to 30 November 2017.

The magnetic field data with the spin-period resolution were obtained by the onboard magnetic field experiment (Matsuoka et al., 2018). The plasma pressure was calculated from proton flux data in the energy range of 9.6–184.2 keV measured by the medium-energy particle experiments-ion mass analyzer (MEP-i; Yokota et al., 2017) instrument. The time resolution of differential fluxes was either ∼8 or ∼16 s. We used data recorded during the normal mode operation, which is basically performed on only inbound passes. In this operation mode, MEP-i obtains the three-dimensional distribution functions, with 16 spin phases, 16 azimuthal channels, and 16 energy steps within a spin. In the other operation mode, the time of flight (TOF) mode operation, the MEP-i obtains high-resolution TOF information, but the resolution of the azimuthal angle is very low (90°). Data obtained from the TOF operation mode are unsuitable for the calculation of the anisotropic pressure; therefore, we excluded the data from the TOF operation mode. All the data from Arase were averaged over 1-min time windows.

We used the *SYM-H** index with 1-min resolution as a proxy for ring current intensity. The *SYM-H** index is the *SYM-H* index corrected for a solar-wind dynamic pressure (P_{SW}), in the same way as the *Dst** index (Burton et al., 1975). The *SYM-H** index here was calculated using the same coefficient as Le et al. (2004): $SYM\text{-}H^* \text{ (nT)} = SYM\text{-}H \text{ (nT)} - 13.5\sqrt{P_{SW}}$ (nPa). The typical value of *SYM-H** during quiet times is ∼ −20 nT. In the current study, we analyzed data from moderately disturbed times, defined by $-80 \leq SYM\text{-}H^* \leq -40$ nT. Quiet times were excluded for two reasons. First, the energy range of the MEP-i mostly covered the population of ring current ions during magnetic storms, while protons with an energy ≥ 200 keV make a significant contribution to plasma pressure during quiet times (e.g., Williams, 1981; Zhao et al., 2015). Second, the sensitivity of the MEP-i began to decrease from September 2017 onward, and large errors in plasma pressure measurements can be made when a count rate is very low. Also, we excluded the strongly disturbed time *SYM-H** ≤ −80 nT to weaken the dependence of the geomagnetic activity, which varies with time. We did not classify the phases of the storms because of the small data coverage. The volume of data collected during the recovery phase was large for the statistical analysis because the duration of the recovery phase is much longer than that of the main phase.

2.2. Averaging Process

Meridional distributions were given by averaging the values in each spatial bin. We used two types of bins.

One is a ρ-z bin in solar magnetic (SM) coordinates, where the ρ axis is $\sqrt{X_{SM}^2 + Y_{SM}^2}$ and the z axis is Z_{SM}. Since the resulting meridional distribution is given in Cartesian coordinates, this sorting is useful for two-dimensional visualization in the meridional plane and the calculation of pressure-driven currents. The satellite was located in the Northern Hemisphere ($z > 0$) for 93% of the total time of used data, and we used only data in the Northern Hemisphere. The bin size was $0.5\,R_E \times 0.5\,R_E$ except for the region of $\rho \geq 4.5\,R_E$ and $0 \leq z \leq 1R_E$. For this exceptional region, a $0.5\,R_E$ bin for the ρ axis and a $1\,R_E$ bin for the z axis were used because the number of data points was very small. Figure 1a shows the distribution of the total time of the data used for the analysis in the ρ-z plane. The data points used in the present study covered an MLAT range of 0–40° and a radial distance of $< 6R_E$. After averaging the data in each bin, we applied a bilinear interpolation by a $0.25\,R_E$ grid, and a simple three-point moving average in each dimension to obtain smooth distributions: $S_{i,j} = (X_{i,j-1} + X_{i-1,j} + X_{i,j} + X_{i+1,j} + X_{i,j+1})/5$, where $S_{i,j}$ is the smoothed distributions and $X_{i,j}$ is the interpolated distributions at ith and jth grid points in ρ and z, respectively.

The other bin is for examining the MLAT distribution in the same L^* (Roederer, 1970) defined as $L^* = \frac{2\pi k_0}{\Phi R_E}$ where k_0 is the Earth's magnetic moment and Φ is the third adiabatic invariant. So L^* is based on the conservation of Φ. The Olson-Pfitzer quiet magnetic field model (Olson & Pfitzer, 1977) was used for the calculation
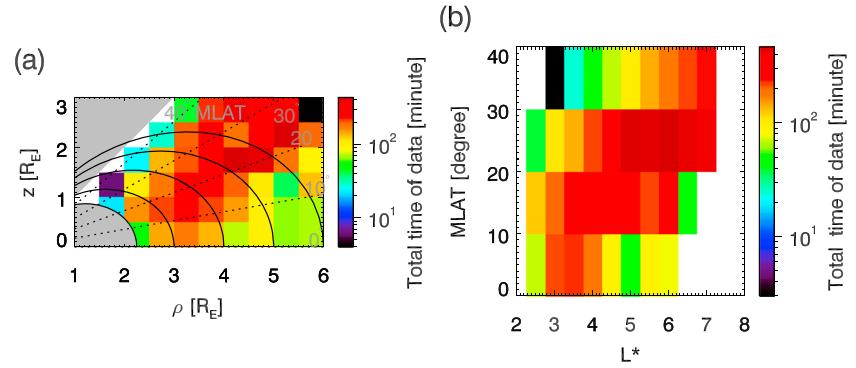
Figure 1. Distribution of the total time of the data used for the analysis in the (a) ρ-z ($\rho = \sqrt{X_{SM}^2 + Y_{SM}^2}$, $z = Z_{SM}$) plane and (b) the L^*-MLAT plane. Black curves show the dipole field lines. Radial grids are drawn at 10° intervals. Regions of MLAT $\geq$ 45° and a dipole $L \leq 2.25$ are masked by gray shading. MLAT = magnetic latitude.

of L^*, which is included in the Arase level-3 orbit data (https://ergsc.isee.nagoya-u.ac.jp/data/ergsc/satellite/erg/orb/l3/; Miyoshi et al., 2018). This L^* definition was adopted by the Panel for Radiation Belt Environment Modeling for a model of the Earth's trapped radiation belts. We used L^* at a local pitch angle of 90° for simplicity because the flux of middle-energy protons is dominant around 90° pitch angle (i.e., pancake distribution) in the inner magnetosphere for most cases (Garcia & Spjeldvik, 1985; Shi et al., 2016; Sibeck et al., 1987). The L^* is slightly smaller than the dipole L, and its difference increases with increasing L^*. At Arase's orbit in the inner magnetosphere ($L^* \leq 6$), the difference is ~0.3 at most. MLAT was calculated with respect to the dipole axis (Z_{SM} axis). The bin size was $0.5 \times 10°$ for L^* and MLAT, respectively. Figure 1b shows the distribution of the total time of the data used for the analysis in the L^*-MLAT plane. The total time of the data was small in the distant region near the equator ($L^* \geq 5$ and $0° \leq$ MLAT $\leq 10°$) and the low-altitude region at a higher latitude ($L^* \leq 4$ and $30° \leq$ MLAT $\leq 40°$) compared with other regions.

2.3. Calculation of Plasma Parameters and Pressure-Driven Current Densities

The plasma pressures perpendicular and parallel to the ambient magnetic field ($P_\perp$, $P_\parallel$) were calculated from the energy (E) and pitch angle (α) distributions of the differential flux $J(E, \alpha)$ obtained by the following formulae (e.g., De Michelis et al., 1999; Menz et al., 2017):

$$P_\perp = \pi \sum_E \sum_\alpha \sqrt{2mE} J(E, \alpha) \sin^3\alpha \Delta E \Delta\alpha,$$

$$P_\parallel = 2\pi \sum_E \sum_\alpha \sqrt{2mE} J(E, \alpha) \cos^2\alpha \sin\alpha \Delta E \Delta\alpha,$$

where m is the mass of a particle, ΔE is the energy channel width, and $\Delta\alpha$ is a pitch angle bin width. We set the pitch angle bin width to 22.5°, just dividing 180° into eight sectors from the magnetic field direction. This pitch angle bin width is nearly equal to the interval of azimuthal channels and spin phases of MEP-i. So all pitch angle bins contain at least one flux observation for a spin regardless of the angle between the spin axis and the magnetic field line. Note that the plasma pressure calculated from the MEP-i was always underestimated due to the pronounced energy coverage limitation in the region $L < 3$, in which the contribution of high-energy protons (>~200 keV) is significant (De Michelis et al., 1999). Nevertheless, it is still useful to examine pressure distributions in the meridional plane relative to equatorial values.

The plasma pressure anisotropy index (A) is defined here as

$$A = \frac{P_\perp}{P_\parallel} - 1,$$

meaning that positive values are $P_\perp > P_\parallel$. Anisotropy A is unreliable if $P_\parallel$ is very small; therefore, we excluded A when $P_\parallel$ was below 0.1 nPa.
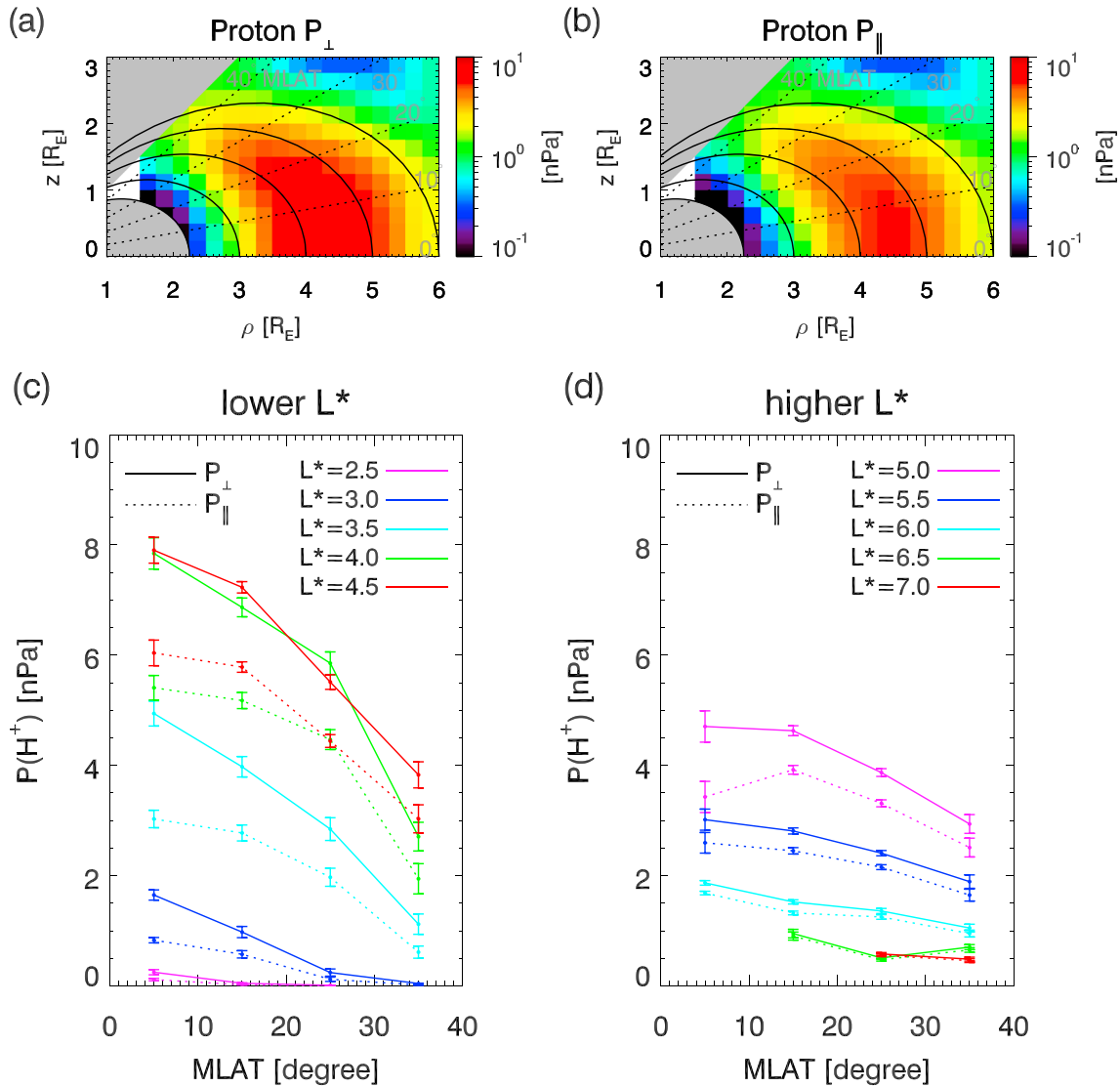
Figure 2. Distributions of (a) perpendicular and (b) parallel plasma pressures in the ρ-z plane. Black curves show the dipole field lines, and radial grids are drawn at 10° intervals. The perpendicular and parallel plasma pressures are shown as a function of MLAT for (c) lower L^*s ($L^* = 2.5$–4.5) and (d) higher L^*s ($L^* = 5$–7). Solid lines show the perpendicular plasma pressure, and dotted lines show the parallel plasma pressure. Error bars denote the standard errors of the mean as the sample standard deviation divided by the square root of the sample size. MLAT = magnetic latitude.

The perpendicular and parallel plasma betas ($\beta_\perp$, $\beta_\parallel$) were defined as the ratio between the plasma pressure and the magnetic pressure, where $B^2/2\mu_0$: B is the magnetic field, and μ_0 is the permeability of free space, as

$$\beta_\perp = \frac{2\mu_0 P_\perp}{B^2}$$

$$\beta_\parallel = \frac{2\mu_0 P_\parallel}{B^2}.$$

The perpendicular current ($j_\perp$) in static equilibrium can be described by the plasma pressure and the magnetic field in the magnetohydrodynamics approximation (Parker, 1957) as

$$\boldsymbol{j}_\perp = \frac{\boldsymbol{B}}{B^2} \times \left[\nabla P_\perp + (P_\parallel - P_\perp)\left(\frac{\boldsymbol{B}}{B} \cdot \nabla\right) \frac{\boldsymbol{B}}{B} \right]. \qquad (1)$$

Note that the magnetic-gradient drift and magnetization currents cancel each other out in this equation. The first term in equation (1) is the pressure-gradient current ($j_{\nabla P}$), which constitutes a significant portion of the ring current. The second term, including $\left(\frac{\boldsymbol{B}}{B} \cdot \nabla\right) \frac{\boldsymbol{B}}{B}$: field-line curvature, is called the curvature current (j_c).
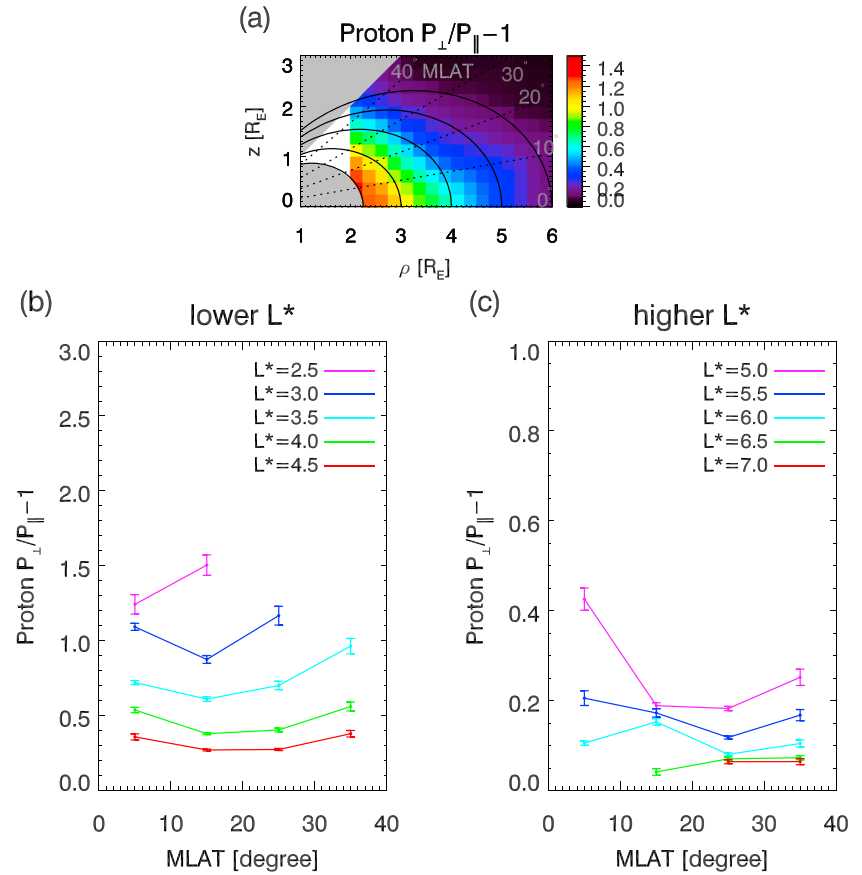
Figure 3. (a) Distribution of the plasma pressure anisotropy in the ρ-z plane. Plasma pressure anisotropy as a function of MLAT for (b) lower L^*s and (c) higher L^*s. The format is the same as for Figure 2. MLAT = magnetic latitude.

The term including $P_\parallel$ corresponds to the curvature drift current, and the term including $P_\perp$ corresponds to the curvature magnetization current. Taking the azimuthal component from equation 1, we obtained the azimuthal currents as

$$j_{\nabla P} = \frac{B_z(\nabla P_\perp)_\rho - B_\rho(\nabla P_\perp)_z}{B^2}$$

$$j_c = (P_\parallel - P_\perp)\left(\frac{\boldsymbol{B} \times (\boldsymbol{B} \cdot \nabla)\boldsymbol{B}}{B^4}\right)_\phi$$

$$= (P_\parallel - P_\perp)\frac{\{B_\rho(\nabla B_\rho)_\rho + B_z(\nabla B_\rho)_z\}B_z - \{B_\rho(\nabla B_z)_\rho + B_z(\nabla B_z)_z\}B_\rho}{B^4}.$$

The field-line curvature can be expressed by the curvature radius R_c which is more intuitively understood as $-\frac{\boldsymbol{R_c}}{R_c^2} = \left(\frac{\boldsymbol{B}}{B} \cdot \nabla\right)\frac{\boldsymbol{B}}{B}$. So j_c also can be written as

$$\boldsymbol{j_c} = -(P_\parallel - P_\perp)\frac{\boldsymbol{B}}{B^2} \times \frac{\boldsymbol{R_c}}{R_c^2}.$$

Taking the azimuthal component, we obtained

$$j_c = -(P_\parallel - P_\perp)\frac{1}{BR_c}.$$

We calculated the current density in the ρ-z plane using the average distributions of the magnetic field and the plasma pressure. The distribution of R_c was also investigated for an interpretation of the distribution of the curvature current.
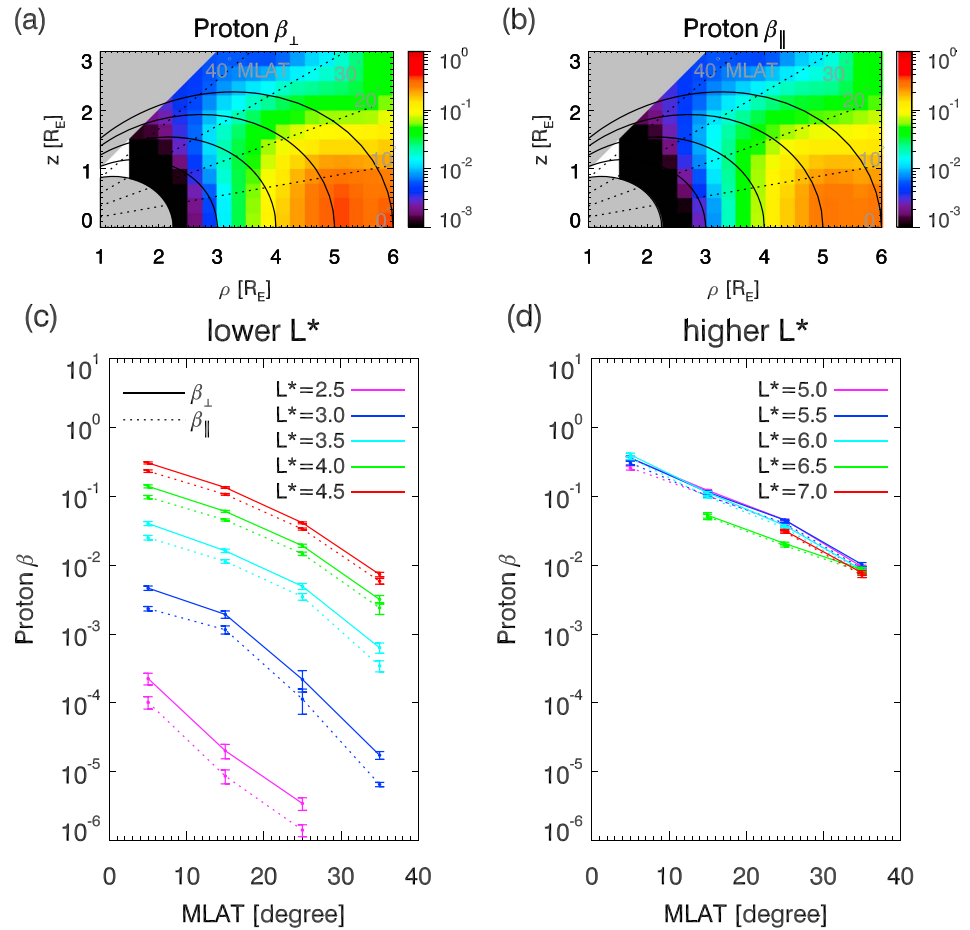
Figure 4. Distribution of (a) perpendicular and (b) parallel plasma betas in the ρ-z plane. Perpendicular and parallel plasma betas as a function of MLAT for (c) lower L^*s and (d) higher L^*s. Solid lines show perpendicular plasma beta, and dotted lines show parallel plasma beta. The format is the same as for Figure 2. MLAT = magnetic latitude.

3. Results

Figure 2 shows the distributions of perpendicular and parallel plasma pressures. In Figures 2a and 2b, the two-dimensional illustrations indicate that the plasma pressures were distributed in a crescent fashion, to align with field lines. There is a peak at $\sim 4.3 R_E$ on the magnetic equator. Figures 2c and 2d show the perpendicular and parallel plasma pressures as a function of MLAT for lower L^*s ($L^* = 2.5$–4.5) and higher L^*s ($L^* = 5$–7), respectively. The plasma pressures decreased with increasing MLAT; for example, at $L^* = 4$, $P_\perp$ at 30° < MLAT < 40° was only 30% of that at 0° < MLAT < 10°. The rate of decrease tended to be large at lower L^*. We discuss the decreasing rate using a model estimation of the field-aligned particle distribution in a later section. For all L^*s, $P_\perp$ is larger than $P_\parallel$ even at higher latitudes.

Figure 3 shows the distributions of the plasma pressure anisotropy (A). As expected from Figure 2, the plasma anisotropy was positive ($P_\perp > P_\parallel$) in the entire meridional plane. The pressure anisotropy at the magnetic equator decreased with radial distance, which is in agreement with previous results (e.g., De Michelis et al., 1999; Lui & Hamilton, 1992). This feature was also shown in off-equatorial regions (Figure 3a), and thus, the pressure anisotropy strongly depends on the radial distance. Figures 3b and 3c show that the pressure anisotropy was not changed largely with MLAT, although there were weak minima around 20° MLAT at $L^* \leq 5$.

Figure 4 shows the distribution of the perpendicular and parallel plasma betas ($\beta_\perp$, $\beta_\parallel$). The plasma betas drastically decreased with decreasing radial distance, which is consistent with the result at the magnetic equator (Lui & Hamilton, 1992). An important feature, shown in Figures 4c and 4d, is that the plasma beta drastically decreased with increasing MLAT. Their magnitude at 30° < MLAT < 40° was 1 or 2 orders
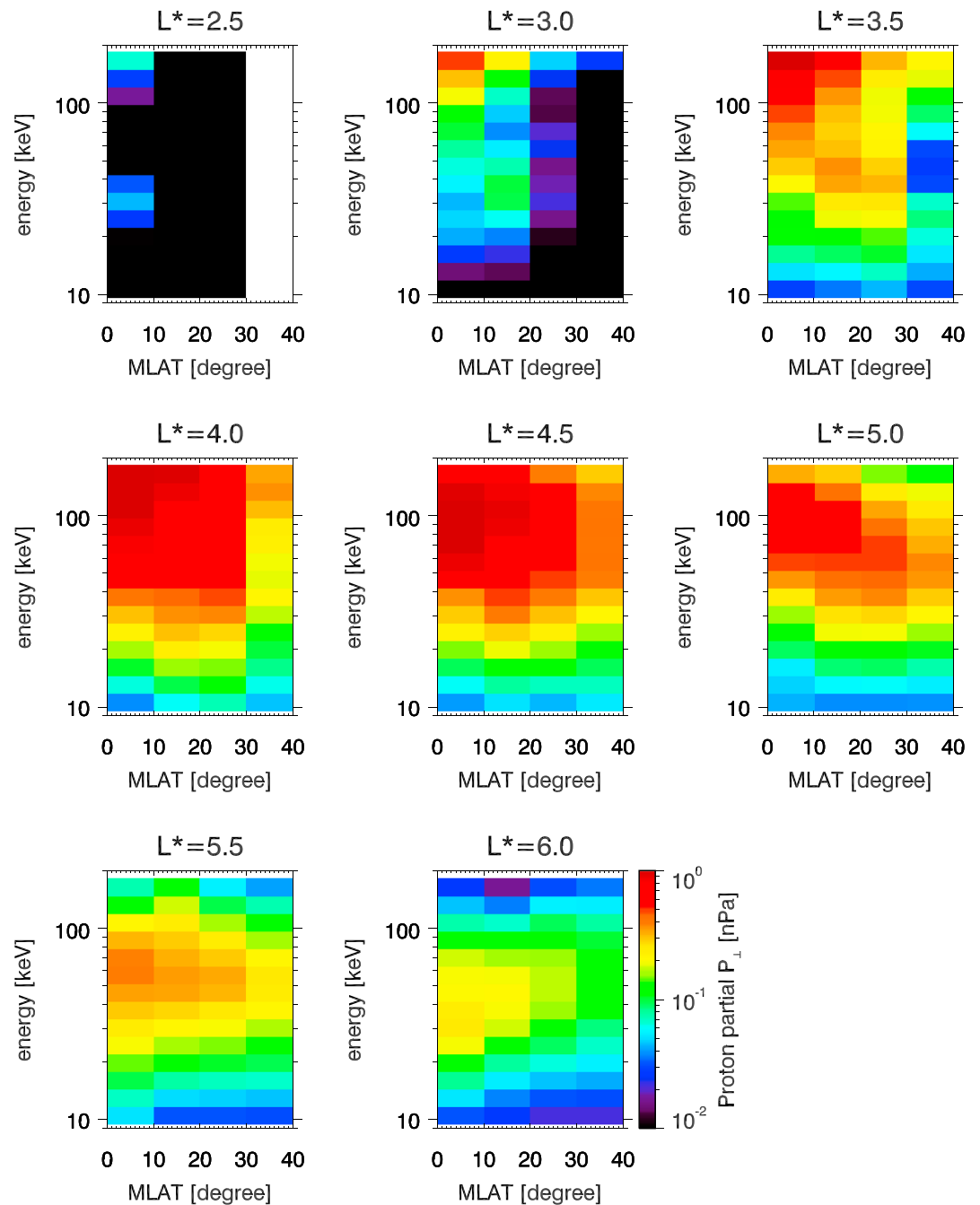
Figure 5. Distribution of the partial perpendicular plasma pressure as a function of MLAT and energy for each L^*. MLAT = magnetic latitude.

smaller than that at $0° <$ MLAT $< 10°$. This is due to a decrease in the plasma pressure and an increase in the magnetic strength with increasing MLAT.

We also investigated the energy dependence of the meridional distribution of the partial plasma pressure. Figure 5 shows the distribution of the partial perpendicular plasma pressure as functions of MLAT and energy for each L^*. The sum of each column corresponds to the total plasma pressure of the MEP-i, as shown in Figure 2. The main energy range that contributed to the total plasma pressure was higher at the lower L^* near the equator, which is consistent with Van Allen probes observations reported by Yue et al. (2018). This tendency was also true in the off-equator region. The increase in the main contributing energy is probably because the perpendicular velocity of protons increases when they are transported inward adiabatically from
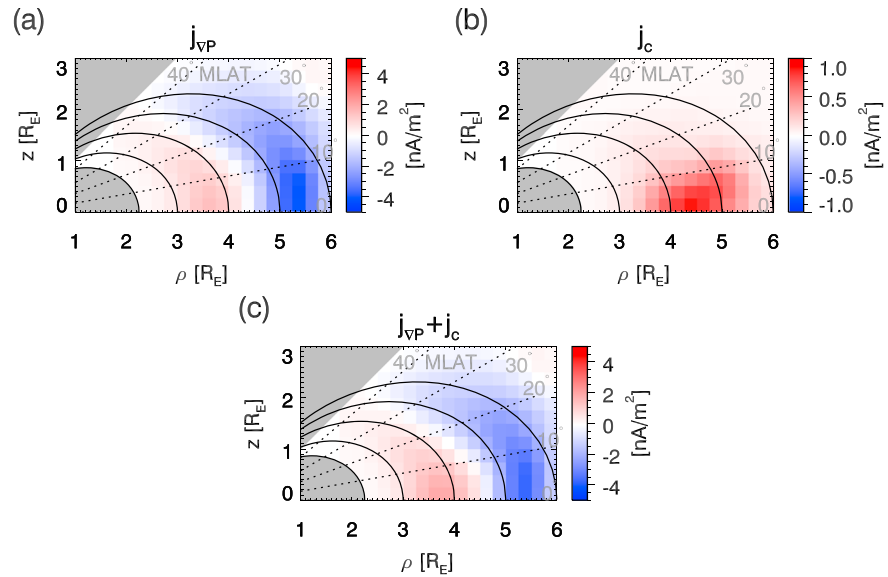
Figure 6. Distributions of (a) pressure-gradient current, (b) curvature current, and (c) total of them in the ρ-z plane (Positive eastward). The format is the same as Figure 2a. MLAT = magnetic latitude.

the magnetotail. The partial plasma pressure decreased monotonically in the energy range of 50–180 keV in $3 \leq L^* \leq 5$. In $3.5 \leq L^* \leq 5$, the partial plasma pressure of 10–50 keV had a peak around 20° MLAT. Keika et al. (2018) showed a similar peak in 10–50 keV during main phases using the data from the Arase satellite.

Figure 6 shows the distribution of pressure-driven currents derived from the pressure and magnetic field distributions. The pressure-gradient current ($j_{\nabla P}$; Figure 6a) flowed westward outside and eastward inside the pressure peak. The westward current was stronger than the eastward current. The peak current densities were 4 nA/m² for the westward current ($\rho \sim 5 R_E$) and 1 nA/m² for the eastward current ($\rho \sim 3.5 R_E$). These features are consistent with the currents derived from the particle data from Active Magnetospheric Particle Tracer Explorer/Charge Composition Explorer observations (Lui et al., 1987). A large portion of pressure-gradient current was distributed over $\sim$ 0–20°. The curvature current (j_c) flows eastward because of $P_\perp > P_\parallel$ with a smaller magnitude (~ 1 nA/m²) than the pressure-gradient current (Figure 6b). Contrary to the pressure-gradient current, the curvature current is limited near the equator within $\sim$ 0–10°. The total pressure-driven current ($j_{\nabla P} + j_c$) almost reflected the pattern of $j_{\nabla P}$ (Figure 6c). The main part of the total pressure-driven current was also distributed over $\sim$ 0–20°, which is in agreement with the currents derived from the curl of the average magnetic fields (Jorgensen et al., 2004; Le et al., 2004).

4. Discussion

4.1. Latitudinal Dependence of Plasma Pressure: Comparison With Theory

As shown in Figure 2, the plasma pressure decreased with increasing MLAT. Based on the theory by Parker (1957), we expected the decrease in pressure to depend on both the magnetic strength and the pressure anisotropy, as shown below. Here we consider a simple condition that particles are trapped in the same flux tube and the particle distribution is in static equilibrium. Parker (1957) demonstrated that the distribution function f at a location s on the same field line can be expressed by $B(s)$ as

$$f(s, \alpha) = C_\alpha \left[\frac{B(0)}{B(s)} \right]^{\frac{\gamma-1}{2}} \sin^\gamma \alpha, \tag{2}$$

where C_α is a constant, $s = 0$ is the magnetic equator, and γ is a power index to show the plasma anisotropy. This means that the shape of $f(s, \alpha)$ is conserved along the field line if the pitch-angle distribution is approximated by $\sin^\gamma \alpha$ function but its amplitude varies with the magnetic field change along the field line. Thus, f relative to the equatorial value becomes $f(s, \alpha)/f(0, \alpha) = \left[B(0)/B(s) \right]^{\frac{\gamma-1}{2}}$. Assuming that f is the distribution function at the representative energy in the energy range for the calculation of the plasma pressure for
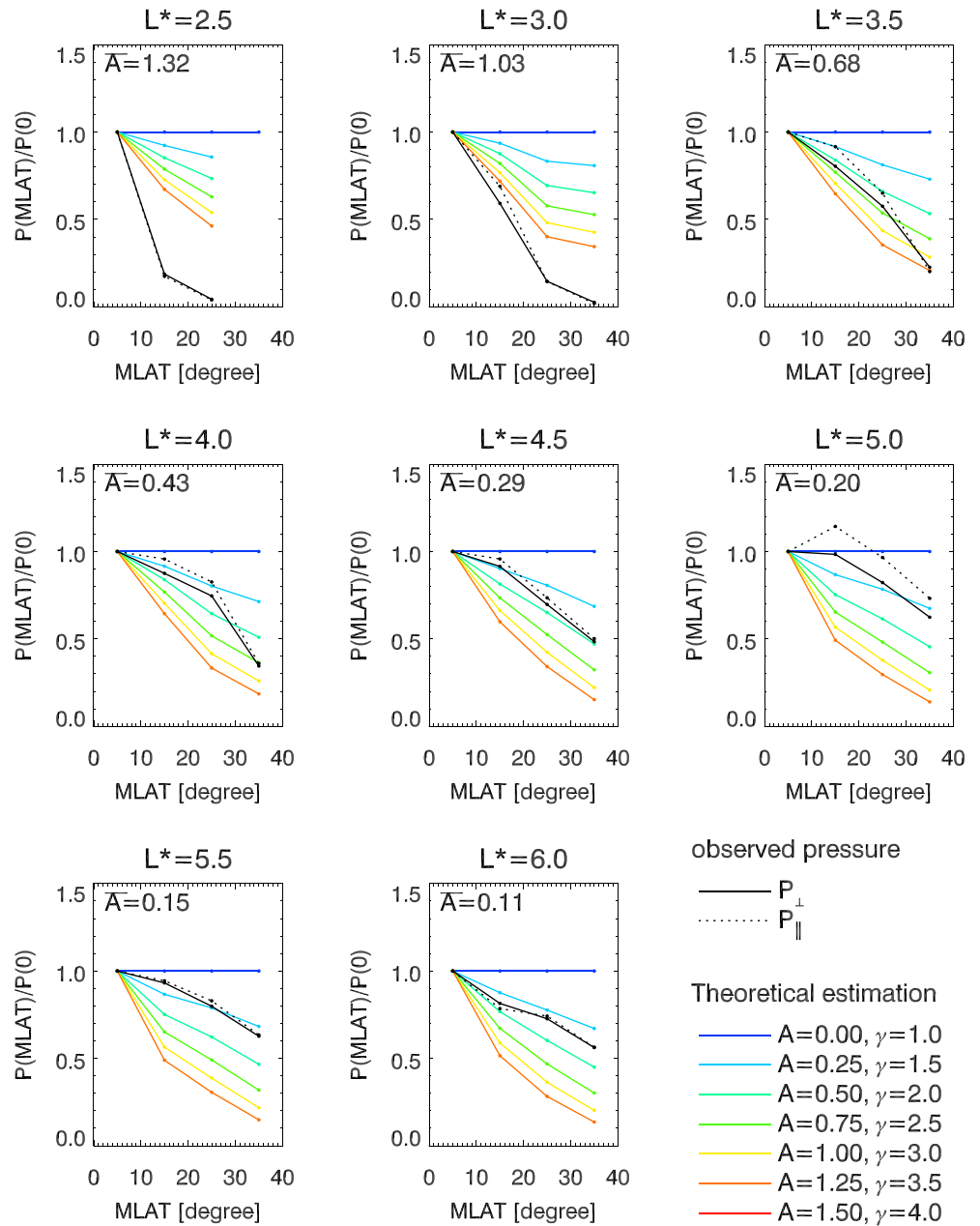
Figure 7. Comparison of plasma pressure variations with MLAT between the particle measurement and the estimation from the magnetic field for each anisotropy. Black lines (solid for $P_\perp$ and dashed for $P_\parallel$) show the observed plasma pressure normalized by the average values in ~ 0–$10°$ MLAT ($P(\text{MLAT})/P(0)$). Colored solid lines show the normalized plasma pressure estimated from the magnetic field for each anisotropy A or corresponding γ. The observed anisotropies averaged over each L^* bin ($\overline{A}$) are shown at the top of each panel. MLAT = magnetic latitude.

simplicity, Sckopke (1966) demonstrated that the anisotropic pressure can be expressed by γ as

$$P_\perp(s) = \frac{\gamma + 1}{\gamma + 2} \epsilon_\gamma(s)$$

$$P_\parallel(s) = \frac{2}{\gamma + 2} \epsilon_\gamma(s),$$

where $\epsilon_\gamma(s)$ is the energy density: $\int \mathrm{d}E \int_0^\pi f(s, \alpha) \mathrm{d}\alpha$. So the relation between A and γ is given by

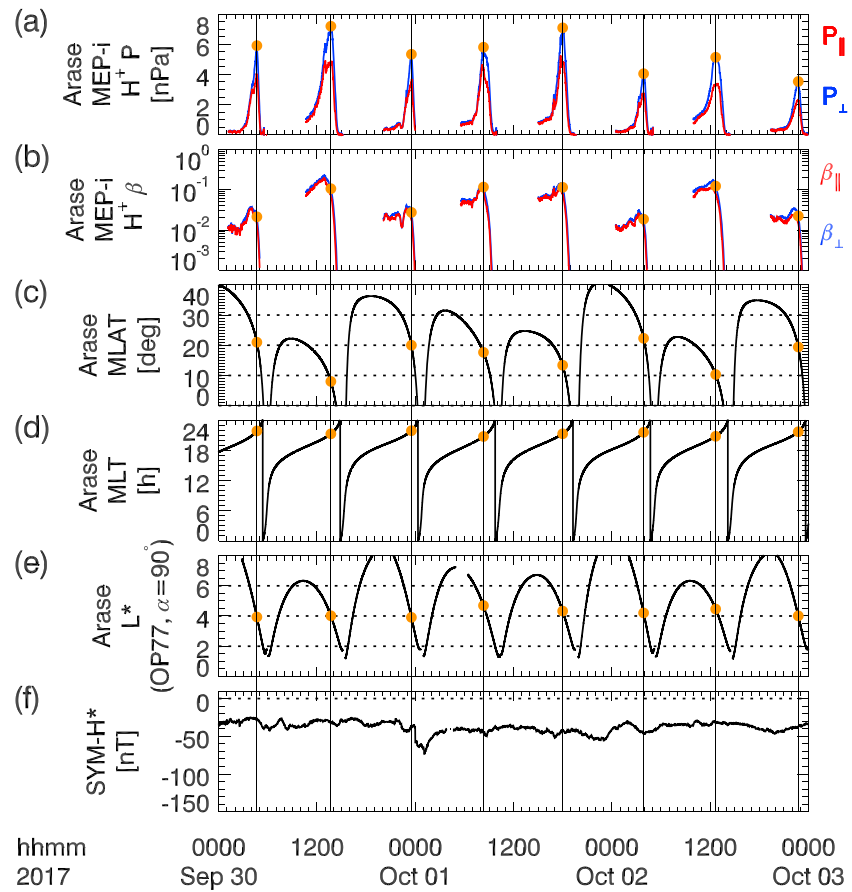$$A = \frac{P_\perp}{P_\parallel} - 1 = \frac{\gamma - 1}{2}. \tag{3}$$

Figure 8. Time series of (a) plasma pressure, (b) plasma beta, (c) magnetic latitude, (d) magnetic local time, and (e) L^* at 90° pitch angle at Arase and (f) *SYM-H** between 30 September and 3 October 2017. The plasma pressure and plasma beta are shown for only the inbound passes. Vertical bars indicate the times of maximum perpendicular plasma pressures for each orbit. Orange dots indicate the values at these times. MEP-i = medium-energy particle experiments-ion mass analyzer; MLAT = magnetic latitude; MLT = magnetic local time.

Under the assumptions of Parker's model, if the pitch angle distribution can be expressed by the $\sin^\gamma \alpha$ shape, the shape of pitch angle distribution does not depend on s but its amplitude is changed. The shape of the pitch angle distribution is determined by γ, and this does not depend on s. Thus, equation (3) indicates that the pressure anisotropy A is constant along the field line under the assumptions.

Since the integral of $f(s, \alpha)$ by α affects only $\sin^\gamma \alpha$, $P_{\perp,\parallel}(s)$ is proportional to $f(s, \alpha)$. Thus, the relation between $P_{\perp,\parallel}(s)$ and $f(s, \alpha)$ is given by

$$\frac{P_{\perp,\parallel}(s)}{P_{\perp,\parallel}(0)} = \frac{f(s, \alpha)}{f(0, \alpha)}.$$

Finally, the plasma pressure normalized by the equatorial value is expressed as

$$\frac{P_{\perp,\parallel}(s)}{P_{\perp,\parallel}(0)} = \left[\frac{B(0)}{B(s)}\right]^A. \tag{4}$$

A similar relation was also derived by Boström (1975).

Figure 7 shows a comparison between the plasma pressures derived from both the measurements and the theory (equation (4)). The black lines (solid lines for $P_\perp$ and dashed lines for $P_\parallel$) show the observed plasma pressure normalized by the average values in ~ 0–$10°$ MLAT. The magnetic field averaged over each L^*-MLAT bin was substituted into equation (4). The estimated values were drawn for $A = 0$–1.5 at 0.25 intervals (or $\gamma = 1$–4 at 0.5 intervals). The measured anisotropy, which was calculated from the MEP-i data and
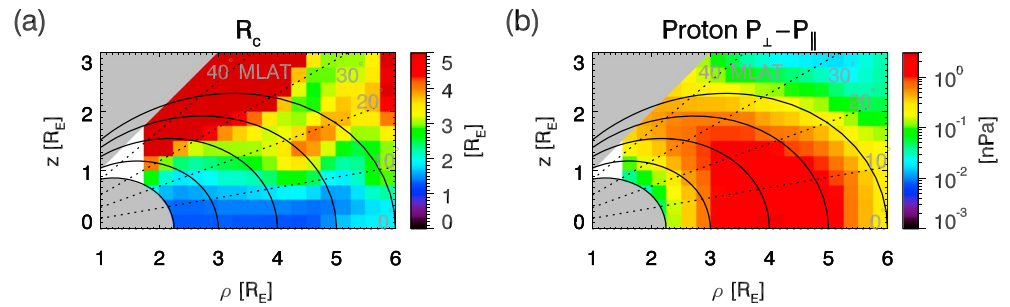
Figure 9. Distribution of (a) the curvature radius (R_c) and (b) the difference between perpendicular and parallel pressures ($P_\perp - P_\parallel$). The format is the same as for Figure 2a. MLAT = magnetic latitude.

averaged over each L^* bin ($\overline{A}$), is displayed at the top of each panel. The MLAT dependence of the observed pressure and average anisotropy roughly agreed with the theory at $L^* = 3.5$–5.5. Alternatively, the observed pressure at $L^* = 2.5$–3 and 6 decreased more steeply than the theoretical results with $\overline{A}$.

Although the inner magnetosphere is not exactly in static equilibrium, the Grad-Shafranov equilibrium equation ($-\nabla P + j \times B = 0$) can be validly assumed because the ring current evolutionary timescale during storm times is much longer than the typical Alfvén transit time, and the flow velocity is slower than Alfvén speed (Voigt & Wolf, 1988; Zaharia et al., 2006). The background magnetic field is determined by the pressure distribution to ensure the equilibrium, and the magnetic field in the inner magnetosphere could be distorted by the pressure enhancement during storm times. As a result, the current L^* definition did not always accurately reflect the actual particle drift shells for a specific situation because the Olson-Pfitzer quiet model does not depend on any inputs associated with particle dynamics in the inner magnetosphere. This could have been the dominant reason for the discrepancies between the observations and the theoretical estimation.

The partial plasma pressures with the higher energy tended to decrease rapidly with increasing MLAT, as shown in Figure 5. This probably occurred because the anisotropy increased with increasing energy (Lui et al., 1990; Shi et al., 2016). Because the partial pressures with the lower energy were expected to gradually decrease, this gradual decrease could have been easily obscured by the above mentioned factors of some of the discrepancies between the observations and the theoretical predictions. In particular, the time variation of lower-energy protons is large because they are often injected into the inner magnetosphere during substorms and decay rapidly by charge exchange (Smith & Bewtra, 1978). In addition, lower-energy particles have a larger MLT (longitudinal) variation because the velocity of their magnetic gradient drift is slower. Thus, the meridional distribution of lower-energy protons can easily be distorted by the MLT variation.

4.2. Latitudinal Dependence of Plasma Parameters in Successive Orbits

The latitudinal dependence of the plasma pressure and plasma beta can affect the interpretation of L^* dependences in successive orbits. Figure 8 shows a good example of how the plasma pressure and plasma beta depended on the magnetic latitude in successive orbits. This example is in the late recovery phase, from 30 September to 3 October 2017, of a storm that started on 27 September 2017. The plasma pressure and plasma beta are only shown for the inbound passes in the premidnight sector. Although *SYM-H** was relatively constant, the plasma pressure and beta significantly varied from orbit to orbit. These changes, which initially appeared to be random, corresponded to changes in the MLAT of each orbit: There is a one-to-one correspondence between an increase in the peak plasma pressure and a decrease in the MLAT. The plasma beta was affected more by the MLAT, and the order of magnitude differed from orbit to orbit, depending on the MLAT. Such variations, due to MLAT, accompanied by the orbital evolution can always overlap the temporal evolution of ring current particles. The L^* at each pressure peak slightly varied with orbits (Figure 8e), but the L^* did not show a one-to-one correspondence to peak pressure values. Therefore, one should be careful to not consider variations due to latitudinal differences as a temporal evolution when examining the L^* dependence of plasma pressure in successive orbits.

4.3. Latitudinal Dependence of Currents

We showed that the latitudinal extent of the curvature current is smaller than that of the pressure-gradient current (Figure 6). Since the factor of $1/B$ is common to both currents, $1/R_c$ and $P_\perp - P_\parallel$ can contribute to this
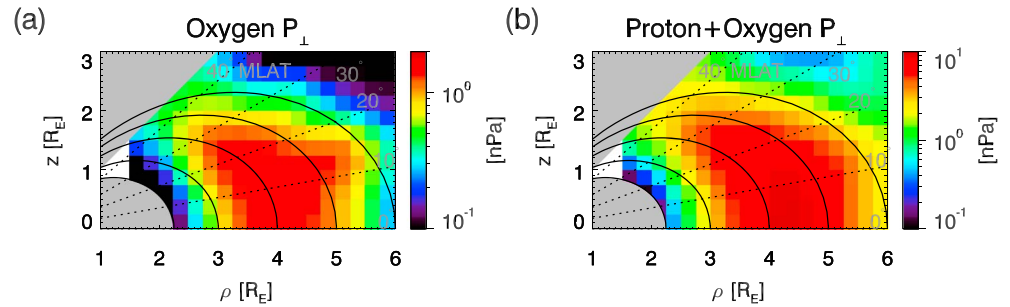
Figure 10. Distribution of the (a) perpendicular plasma pressure of oxygen ions and (b) the total perpendicular plasma pressure combined with protons and oxygen ions. The format is the same as for Figure 2a. MLAT = magnetic latitude.

difference. Figure 9a shows the distribution of the curvature radius calculated from the average distribution of the measured magnetic field. The curvature radius is smallest at the magnetic equator. This is a feature of a dipole magnetic field, and the curvature radius is analytically given by $R_c = \frac{r(1+3\sin^2\lambda)^{3/2}}{3\cos\lambda(1+\sin^2\lambda)}$, where r is the radial distance and λ is the magnetic latitude (Lui et al., 1987). In addition, the current sheet near the magnetic equator creates a field distortion and decreases the magnetic curvature radius at the equator. Figure 9b shows that $P_\perp - P_\parallel$ decreases with increasing MLAT. This is because the plasma pressure is largest at the magnetic equator, and the anisotropy is not changed significantly with MLAT.

Region 2 field-aligned current (R2 FAC) during storms is considered to be connected to the partial ring current (see review by Ganushkina et al., 2018, and references therein). Imajo et al. (2018) showed that storm-time R2 FAC is generated mainly in the region below 20–30° MLAT, based on the conservation of the current between the magnetosphere and the ionosphere. The current study's result showed that a large portion of the azimuthal current is distributed over the region below $\sim$ 20° MLAT (Figure 6c). This indicates that the storm-time R2 FAC is connected to the azimuthal current in the inner magnetosphere below $\sim$ 20° MLAT.

4.4. Contribution of Oxygen Ions to Plasma Pressure

Oxygen ions make a substantial contribution to total plasma pressure and currents in the inner magnetosphere during intense storms (see review by Keika et al., 2013). Since the oxygen pressure is highly variable depending on the geomagnetic activity and storm phases, its spatial distribution is easily affected by temporal variations. We applied the same analysis to the oxygen pressure as shown in Figure 10a. Its distribution was not the same as that of the protons, and there were peaks at $\sim$ 10° and $\sim$ 20° MLAT. It was not clear whether this particular distribution reflected an actual spatial distribution or the effects of large temporal variations. However, because the magnitude of the oxygen pressure was only on average $\sim$20% of the proton pressure, the distribution of the total plasma pressure combined with the proton and oxygen pressure (Figure 10b) was only similar to that of the proton plasma pressure, as shown in Figure 2a. Therefore, the relative distributions of the pressure-driven currents were only slightly modified by adding the oxygen plasma pressure. This indication is in terms of average distributions, and it should be noted that the oxygen plasma pressure could be dominant if we could obtain a snapshot of the meridional distribution at a specific time.

5. Summary

Plasma pressure, anisotropy, and beta value in the inner magnetosphere have been well examined by previous studies in terms of L value and MLT distributions; however, their meridional distributions have not yet been established by observation. Because the Arase satellite has a large inclination of 31°, it covers $-40° \leq$ MLAT $\leq 40°$ and a radial distance of $< 6R_E$. We examined the average meridional distributions of proton plasma parameters and pressure-driven currents in the nightside (20–04 hr MLT) inner magnetosphere during moderately disturbed times ($-80 \leq SYM\text{-}H^* \leq -40$ nT) using Arase satellite ion measurements covering the energy range of 10–180 keV.

We found that the perpendicular and parallel plasma pressures decreased significantly with MLAT. The plasma pressure on the same L^* shell at 30–40° MLAT was about 10–60% of that at 0–10°, and the percentage of decrease was larger on lower L^* shells. The pressure anisotropy ($\frac{P_\perp}{P_\parallel} - 1$) decreased with radial distance increases and showed a weak dependence on MLAT. The perpendicular plasma beta decreased rapidly with

MLAT; its magnitude at 30° < MLAT < 40° was 1 or 2 orders smaller than that at 0° < MLAT < 10°. These variations with MLAT also appeared from orbit to orbit in a time series plot. We compared the observed plasma pressure distribution with the theory of field-aligned particle distribution proposed by Parker (1957). The plasma pressure normalized by the value at 0° < MLAT < 10° predicted from the magnetic strength and anisotropy was roughly consistent with the observed plasma pressure for $L^* = 3.5$–5.5.

We calculated the meridional distribution of a pressure-driven current consisting of a pressure-gradient current and a curvature current using the average distributions of the magnetic field and plasma pressure. A large portion of pressure-gradient current was distributed over ∼ 0–20°. Contrary to the pressure-gradient current, the curvature current was limited near the equator within ∼ 0–10°. This narrow latitudinal extent occurred because the magnetic curvature is smallest and the magnitude of the plasma pressure is largest at the magnetic equator. The total distribution of pressure-gradient current and the curvature current was similar to that of the pressure-gradient current only because the magnitude of the pressure-gradient current was much larger than that of the curvature current. The latitudinal extent of the total current derived from the particle measurements was consistent with that derived from the curl of average magnetic fields (Jorgensen et al., 2004; Le et al., 2004).

The ring current particle population depends on the MLAT as well as the MLT, L value, and temporal evolution of geomagnetic activity. We suggest that the MLAT dependence should be considered when examining the L dependence of plasma parameters and currents in successive orbits.

References

Boström, R. (1975). Mechanisms for driving Birkeland currents. In B. Hultqvist, & L. Stenflo (Eds.), *Physics of the hot plasma in the magnetosphere* (pp. 341–362). Boston, MA: Springer US. https://doi.org/10.1007/978-1-4613-4437-7_16

Burton, R. K., McPherron, R. L., & Russell, C. T. (1975). An empirical relationship between interplanetary conditions and Dst. *Journal of Geophysical Research*, *80*(31), 4204–4214. https://doi.org/10.1029/JA080i031p04204

C:son Brandt, P., Roelof, E., Ohtani, S., Mitchell, D., & Anderson, B. (2004). IMAGE/HENA: Pressure and current distributions during the 1 October 2002 storm. *Advances in Space Research*, *33*(5), 719–722. https://doi.org/10.1016/S0273-1177(03)00633-1

Chandrasekhar, S., Kaufman, A. N., & Watson, K. M. (1958). The stability of the pinch. *Proceedings of the Royal Society of London. Series A. Mathematical and Physical Sciences*, *245*(1243), 435–455. https://doi.org/10.1098/rspa.1958.0094

Cornwall, J. M., Coroniti, F. V., & Thorne, R. M. (1970). Turbulent loss of ring current protons. *Journal of Geophysical Research*, *75*(25), 4699–4709. https://doi.org/10.1029/JA075i025p04699

Daglis, I. A., Sarris, E. T., & Wilken, B. (1993). AMPTE/CCE observations of the ion population at geosynchronous altitudes. *Annales Geophysicae*, *11*, 685–696. https://doi.org/10.1029/2002GL015430

De Michelis, P., Daglis, I. A., & Consolini, G. (1997). Average terrestrial ring current derived from AMPTE/CCE-CHEM measurements. *Journal of Geophysical Research*, *102*(A7), 14,103–14,111. https://doi.org/10.1029/96JA03743

De Michelis, P., Daglis, I. A., & Consolini, G. (1999). An average image of proton plasma pressure and of current systems in the equatorial plane derived from AMPTE/CCE-CHEM measurements. *Journal of Geophysical Research*, *104*(A12), 28,615–28,624. https://doi.org/10.1029/1999JA900310

Ebihara, Y., Ejiri, M., Nilsson, H., Sandahl, I., Milillo, A., Grande, M., et al. (2002). Statistical distribution of the storm-time proton ring current: POLAR measurements. *Geophysical Research Letters*, *29*(20), 1969. https://doi.org/10.1029/2002GL015430

Ganushkina, N. Y., Liemohn, M. W., & Dubyagin, S. (2018). Current systems in the Earth's magnetosphere. *Reviews of Geophysics*, *56*, 309–332. https://doi.org/10.1002/2017RG000590

Garcia, H. A., & Spjeldvik, W. N. (1985). Anisotropy characteristics of geomagnetically trapped ions. *Journal of Geophysical Research*, *90*(A1), 347–358. https://doi.org/10.1029/JA090iA01p00347

Imajo, S., Nosé, M., Matsuoka, A., Kasahara, S., Yokota, S., Teramoto, M., et al. (2018). Magnetosphere-ionosphere connection of storm-time region-2 field-aligned current and ring current: Arase and AMPERE observations. *Journal of Geophysical Research: Space Physics*, *123*, 9545–9559. https://doi.org/10.1029/2018JA025865

Jordanova, V. K., & Miyoshi, Y. (2005). Relativistic model of ring current and radiation belt ions and electrons: Initial results. *Geophysical Research Letters*, *32*, L14104. https://doi.org/10.1029/2005GL023020

Jorgensen, A. M., Spence, H. E., Hughes, W. J., & Singer, H. J. (2004). A statistical study of the global structure of the ring current. *Journal of Geophysical Research*, *109*, A12204. https://doi.org/10.1029/2003JA010090

Keika, K., Kasahara, S., Yokota, S., Hoshino, M., Seki, K., Nosé, M., et al. (2018). Ion energies dominating energy density in the inner magnetosphere: Spatial distributions and composition, observed by Arase/MEP-i. *Geophysical Research Letters*, *45*, 12,153–12,162. https://doi.org/10.1029/2018GL080047

Keika, K., Kistler, L. M., & Brandt, P. C. (2013). Energization of O$^+$ ions in the Earth's inner magnetosphere and the effects on ring current buildup: A review of previous observations and possible mechanisms. *Journal of Geophysical Research: Space Physics*, *118*, 4441–4464. https://doi.org/10.1002/jgra.50371

Le, G., Russell, C., & Takahashi, K. (2004). Morphology of the ring current derived from magnetic field observations. *Annales Geophysicae*, *22*(4), 1267–1295.

Lui, A. T. Y. (2003). Inner magnetospheric plasma pressure distribution and its local time asymmetry. *Geophysical Research Letters*, *30*(16), 1846. https://doi.org/10.1029/2003GL017596

Lui, A. T. Y., & Hamilton, D. C. (1992). Radial profiles of quiet time magnetospheric parameters. *Journal of Geophysical Research*, *97*(A12), 19,325–19,332. https://doi.org/10.1029/92JA01539

Lui, A. T. Y., McEntire, R. W., & Krimigis, S. M. (1987). Evolution of the ring current during two geomagnetic storms. *Journal of Geophysical Research*, *92*(A7), 7459–7470. https://doi.org/10.1029/JA092iA07p07459

Lui, A. T. Y., McEntire, R. W., Sibeck, D. G., & Krimigis, S. M. (1990). Recent findings on angular distributions of dayside ring current energetic ions. *Journal of Geophysical Research*, *95*(A12), 20,839–20,851. https://doi.org/10.1029/JA095iA12p20839

Matsuoka, A., Teramoto, M., Nomura, R., Nosé, M., Fujimoto, A., Tanaka, Y., et al. (2018). The ARASE (ERG) magnetic field investigation. *Earth Planets Space*, *70*(1), 43. https://doi.org/10.1186/s40623-018-0800-1

McEntire, R. W., Lui, A. T. Y., Krimigis, S. M., & Keath, E. P. (1985). AMPTE/CCE energetic particle composition measurements during the September 4, 1984 magnetic storm. *Geophysical Research Letters*, *12*(5), 317–320. https://doi.org/10.1029/GL012i005p00317

Menz, A. M., Kistler, L. M., Mouikis, C. G., Spence, H. E., Skoug, R. M., Funsten, H. O., et al. (2017). The role of convection in the buildup of the ring current pressure during the 17 March 2013 storm. *Journal of Geophysical Research: Space Physics*, *122*, 475–492. https://doi.org/10.1002/2016JA023358

Miyoshi, Y., Hori, T., Shoji, M., Teramoto, M., Chang, T. F., Segawa, T., et al. (2018). The ERG Science Center. *Earth, Planets and Space*, *70*(1), 96. https://doi.org/10.1186/s40623-018-0867-8

Miyoshi, Y., Shinohara, I., Takashima, T., Asamura, K., Higashio, N., Mitani, T., et al. (2018). Geospace exploration project ERG. *Earth, Planets and Space*, *70*(1), 101. https://doi.org/10.1186/s40623-018-0862-0

Olson, W. P., & Pfitzer, K. (1977). Magnetospheric magnetic field modeling (*Annual Science Report F44620-75-c-0033*). Arlington, Va.: Air Force Office of Science Research.

Parker, E. N. (1957). Newtonian development of the dynamical properties of ionized gases of low density. *Physical Review*, *107*, 924–933. https://doi.org/10.1103/PhysRev.107.924

Roederer, J. G. (1970). *Dynamics of geomagnetically trapped radiation*. New York: Cambridge University Press.

Roelof, E. C. (1989). Remote sensing of the ring current using energetic neutral atoms. *Advances in Space Research*, *9*(12), 195–203. https://doi.org/10.1016/0273-1177(89)90329-3

Roelof, E., Brandt, P. C., & Mitchell, D. (2004). Derivation of currents and diamagnetic effects from global plasma pressure distributions obtained by IMAGE/HENA. *Advances in Space Research*, *33*(5), 747–751. https://doi.org/10.1016/S0273-1177(03)00638-0

Sckopke, N. (1966). A general relation between the energy of trapped particles and the disturbance field near the Earth. *Journal of Geophysical Research*, *71*(13), 3125–3130. https://doi.org/10.1029/JZ071i013p03125

Shi, R., Summers, D., Ni, B., Manweiler, J. W., Mitchell, D. G., & Lanzerotti, L. J. (2016). A statistical study of proton pitch angle distributions measured by the radiation belt storm probes ion composition experiment. *Journal of Geophysical Research: Space Physics*, *121*, 5233–5249. https://doi.org/10.1002/2015JA022140

Sibeck, D. G., McEntire, R. W., Lui, A. T. Y., & Krimigis, S. M. (1987). A statistical study of ion pitch angle distributions. In A. T. Y. Lui (Ed.), *Magnetotail physics* pp. 225–230. Baltimore, Maryland: Johns Hopkins Press.

Smith, P. H., & Bewtra, N. K. (1978). Charge exchange lifetimes for ring current ions. *Space Science Reviews*, *22*(3), 301–318. https://doi.org/10.1007/BF00239804

Summers, D., & Shi, R. (2015). Limitation of energetic ring current ion spectra. *Journal of Geophysical Research: Space Physics*, *120*, 7374–7389. https://doi.org/10.1002/2015JA021482

Voigt, G. H., & Wolf, R. A. (1988). Quasi-static magnetospheric MHD processes and the "ground state" of the magnetosphere. *Reviews of Geophysics*, *26*(4), 823–843. https://doi.org/10.1029/RG026i004p00823

Williams, D. (1981). Ring current composition and sources: An update. *Planetary and Space Science*, *29*(11), 1195–1203. https://doi.org/https://doi.org/10.1016/0032-0633(81)90124-0

Yokota, S., Kasahara, S., Mitani, T., Asamura, K., Hirahara, M., Takashima, T., et al. (2017). Medium-energy particle experiments–ion mass analyzer (MEP-i) onboard ERG (Arase). *Earth Planets Space*, *69*(1), 172. https://doi.org/10.1186/s40623-017-0754-8

Yue, C., Bortnik, J., Li, W., Ma, Q., Gkioulidou, M., Reeves, G. D., et al. (2018). The composition of plasma inside geostationary orbit based on Van Allen Probes observations. *Journal of Geophysical Research: Space Physics*, *123*, 6478–6493. https://doi.org/10.1029/2018JA025344

Zaharia, S., Jordanova, V. K., Thomsen, M. F., & Reeves, G. D. (2006). Self-consistent modeling of magnetic fields and plasmas in the inner magnetosphere: Application to a geomagnetic storm. *Journal of Geophysical Research*, *111*, A11S14. https://doi.org/10.1029/2006JA011619

Zhao, H., Li, X., Baker, D. N., Fennell, J. F., Blake, J. B., Larsen, B. A., et al. (2015). The evolution of ring current ion energy density and energy content during geomagnetic storms based on Van Allen Probes measurements. *Journal of Geophysical Research: Space Physics*, *120*, 7493–7511. https://doi.org/10.1002/2015JA021533